COMMUNICATION

Solar Flow Batteries

ADVANCED
ENERGY
MATERIALS

www.advenergymat.de

A Long Lifetime Aqueous Organic Solar Flow Battery

Wenjie Li, Emily Kerr, Marc-Antoni Goulet, Hui-Chun Fu, Yuzhou Zhao, Ying Yang, Atilla Veyssal, Jr-Hau He, Roy G. Gordon, Michael J. Aziz, and Song Jin*

Monolithically integrated solar flow batteries (SFBs) hold promise as compact stand-alone energy systems for off-grid solar electrification. Although considerable research is devoted to studying and improving the round-trip efficiency of SFBs, little attention is paid to the device lifetime. Herein, a neutral pH aqueous electrolyte SFB with robust organic redox couples and inexpensive silicon-based photoelectrodes is demonstrated. Enabled by the excellent stability of both electrolytes and protected photoelectrodes, this SFB device exhibits not only unprecedented stable continuous cycling performance over 200 h but also a capacity utilization rate higher than 80%. Moreover, through comprehensive study on the working mechanisms of SFBs, a new theory based on instantaneous solar-to-output electricity efficiency toward more optimized device design is developed and a significantly improved solar-to-output electricity efficiency of 5.4% from single-junction silicon photoelectrodes is realized. The design principles presented in this work for extending device lifetime and boosting round trip energy efficiency will make SFBs more competitive for off-grid applications.

W. Li, Y. Zhao, Prof. Y. Yang, A. Veyssal, Prof. S. Jin
Department of Chemistry
University of Wisconsin-Madison
1101 University Avenue, Madison, WI 53706, USA
E-mail: jin@chem.wisc.edu

E. Kerr, Prof. R. G. Gordon
Department of Chemistry and Chemical Biology
Harvard University
Cambridge, MA 02138, USA

Dr. M.-A. Goulet, Prof. R. G. Gordon, Prof. M. J. Aziz
John A. Paulson School of Engineering and Applied Sciences
Harvard University
Cambridge, MA 02138, USA

Dr. H.-C. Fu, Prof. J.-H. He
Division of Computer
Electrical and Mathematical Sciences and Engineering
King Abdullah University of Science and Technology
Thuwal 23955-6900, Saudi Arabia

Prof. Y. Yang
Shaanxi Provincial Key Laboratory of Electroanalytical Chemistry
Key Laboratory of Synthetic and Natural Functional Molecule Chemistry
of the Ministry of Education
College of Chemistry and Materials Science
Northwest University
Xi'an, Shaanxi 710127, P. R. China

The ORCID identification number(s) for the author(s) of this article can be found under https://doi.org/10.1002/aenm.201900918.

DOI: 10.1002/aenm.201900918

The monolithic integration of solar energy conversion and electrochemical energy storage offers a practical solution to provide uninterruptable power supply on demand regardless of the ebb and flow of solar irradiation. Although connecting photovoltaics (PVs) with batteries, as adopted by some solar farms nowadays,[1] can provide the same uninterrupted power supply, the high capital cost and large footprint of two separate devices limit the market cases feasible for this option.[2] In contrast, integrated solar energy conversion and storage may represent a more compact, efficient, and cost-effective approach for off-grid electrification.[3]

Among the many different types of "solar rechargeable battery" devices that have been reported[3,4] since the first demonstration in 1976,[5] integrated solar flow batteries (SFBs) hold great promises for practical applications because the solar component shares the same liquid electrolyte as the energy storage component,[6] which is based on redox flow batteries (RFBs) and can be easily scaled up.[2b] Despite the significant progress, most of such integrated devices suffer from some common scientific and technical issues.[4a,7] The first question one typically asks about any "solar device" is the efficiency. Due to the intrinsic efficiency limits of the solar energy conversion components and the working voltage mismatch between the solar energy conversion component and electrochemical energy storage component, the round-trip efficiency (i.e., solar-to-output electricity efficiency, SOEE) of most previously reported solar rechargeable devices rarely exceeded 5%.[3a,4a,7,8] It was recently demonstrated that by monolithically integrating III–V tandem junction solar cells with properly voltage matched RFBs, the integrated SFB device can deliver a SOEE of 14.1%.[9] Importantly, this comprehensive study[9] also revealed a set of general design principles that can further boost the SFB's efficiency. Primary among them is that the formal potential difference of selected redox couples needs to be closely matched with the photovoltage of the photoelectrodes at the maximum power point. Although III–V tandem junction solar cells can enable unprecedented high SOEE, the manufacturing cost for them ($40 W^{-1} to over $100 W^{-1})[10] is too high for practical applications. The most widely produced crystalline silicon-based solar cells have the cost of $0.15 to $0.25 W^{-1} after decades of research and commercial deployment,[10] thus are a good candidate for practical SFBs owing to its high abundance and decent PV efficiency.

ADVANCED
SCIENCE NEWS
www.advancedsciencenews.com

ADVANCED
ENERGY
MATERIALS
www.advenergymat.de

On the other hand, another important aspect, device lifetime, has received much less attention than efficiency, which could be partially attributed to different types of challenges involved in achieving longer device lifetime. As summarized in Table S1 (Supporting Information), none of the existing integrated SFB devices has shown a stable continuous cycling performance longer than 50 h.[4a] Generally, there are two major challenges preventing those devices from reaching long device lifetime. First, many redox active species, although they undergo facile redox reactions, are chemically or electrochemically unstable for long-term energy storage.[11] The 1,2-benzoquinone-3,5-disulfonic acid (BQDS) redox couple used in a previous prototype SFB device[8b] and other RFB works[12] is an example of such unstable redox species. It has been shown that the BQDS molecule is particularly susceptible to decomposition by Michael addition.[12b] Second, the photocorrosion of semiconductor photoelectrodes by aqueous electrolytes has long been one of the biggest obstacles to the practical application of photoelectrochemical (PEC) cells.[13] This has prompted strategies such as the deposition of inert protection layers and utilization of less corrosive electrolytes to balance the lifetime and efficiency of photoelectrodes.[13c,14]

As pointed out by various recent reports, the chemical cost of redox active materials would eventually become a tiebreaker for future RFBs with rapid technology development.[15] Although a detailed cost analysis for SFBs has not been performed, the cost of active materials is likely to be a significant contributor to the cost of SFB systems as well. Consequently, redox couples that are based on earth abundant elements, which include many organic and organometallic species, are attractive for developing SFBs. In comparison to the more mature inorganic redox species that have been commercially deployed (such as vanadium),[2a] organic and organometallic compounds tend to be more prone to chemical decomposition.[11c] However, one of the most stable organic RFBs reported so far[11d,16] is based on bis((3-trimethylammonio)propyl) (BTMAP) functionalized viologen (Vi) and ferrocene (Fc) redox couples, which exhibits an exceptionally low capacity fade rate of 11.3% year^{-1}. Such excellent stability of these molecules has been attributed to the suppression of a bimolecular degradation mechanism by the strong electrostatic repulsion induced by the positive charge on the BTMAP side chains.[16c] Moreover, these molecules also exhibit very low permeabilities across anion exchange membranes, possibly through enhanced charge and size exclusion. The good stability, high solubility in neutral solutions, and suitable formal potential of the BTMAP redox couples make them a perfect fit for the long lifetime SFB.

In this paper, we report a neutral pH solar flow battery with a stable continuous cycling performance over 200 h (100 cycles). This long lifetime device is built by integrating well-protected silicon photoelectrodes with robust BTMAP functionalized organic viologen and ferrocene redox couples in neutral aqueous solutions. Moreover, building on a comprehensive study on the working mechanisms of SFBs, we introduce a new concept, instantaneous SOEE (SOEE$_{ins}$), and show that understanding of instantaneous SOEE and more optimized SFB design can greatly boost the overall SOEE from 1.7[8b] to 5.4% even though the same silicon photoelectrode design is used.

We synthesized bis((3-trimethylammonio)propyl)-ferrocene dichloride (BTMAP-Fc) and bis(3-trimethylammonio)propyl viologen tetrachloride (BTMAP-Vi) following the method reported by Beh et al.[16c] and characterized their electrochemical properties using three-electrode cyclic voltammetry, steady-state linear scan voltammetry, and two-electrode RFB cycling. Cyclic voltammograms show a formal potential difference of 0.735 V between these two redox couples (**Figure 1**A), which can be used to estimate the cell potential (E_{cell}) of the RFBs and SFBs built with these redox couples. As discussed later, although this E_{cell} does not fully utilize the stability window constrained by water splitting, it can be well matched with the photovoltage produced by two silicon photoelectrodes. We also confirmed good redox kinetics of both redox couples by steady-state linear sweep voltammetry with rotating disk electrode (Figure S1, Supporting Information). Then RFB tests were performed in the SFB device[9] we developed without the photoelectrodes. 0.2 M of BTMAP-Fc and 0.2 M of BTMAP-Vi were used as anolyte and catholyte, respectively, both with 1 M of NaCl as supporting electrolyte. The galvanostatic cycling tests were performed at six different current densities from 5 to 50 mA cm^{-2} (Figure 1B). The RFB showed excellent Coulombic efficiencies (CE) of >99.9% at all rates (Figure 1C). We noticed that the energy efficiency is rather limited at high cycling rates as a result of high area specific resistance (ASR) of the Selemion DSV anion exchange membrane used. The lack of a high conductivity and low permeability anion exchange membrane remains a common issue in the development of high-performance RFBs.[17] However, due to the greater limitation on current density of the photoelectrode and the smaller area of the photoelectrode (≈1.2 cm^2) than that of RFB electrode (4 cm^2), the SFB device usually does not need to be operated at a current density higher than 10 mA cm^{-2} based on the area of RFB electrode. (In practical applications, the areal size of photoelectrodes should be close to that of RFB electrodes, which can be realized with further device engineering and optimization.) Therefore, a high energy efficiency (>90%) for the electrochemical energy storage and redelivery process is guaranteed based on Figure 1C.

To perform bias-free photocharging and on-demand electrochemical discharging of the BTMAP redox couples, we built the SFB device by integrating two carbon felt electrodes and two silicon photoelectrodes in close contact (**Figure 2**A), similar to the "zero-gap" device design commonly seen in RFBs.[18] Such design allows us to switch the function of the device between three different modes: RFB mode, solar cell mode, and solar recharge mode, and thus fulfill all the requirements for a stand-alone solar electrification system. As illustrated in Figure 2B, the two photoelectrodes used in the SFB device were both fabricated by forming internal solid-state p-n junction on n-type silicon substrates, but with opposite polarity so that they can be implemented as photoanode (n$^+$np$^+$-Si) and photocathode (p$^+$nn$^+$-Si), respectively. Solar illumination comes from the n$^+$ side for photoanode and p$^+$ side for photocathode in a bifacial fashion. We further deposited a Ti/TiO$_2$/Pt (5 nm/40 nm/5 nm) layer on the back side of the photoelectrodes, where solution would be in direct contact, to protect silicon from photocorrosion. Previous reports have shown that TiO$_2$ protected Si photoelectrodes can be continuously
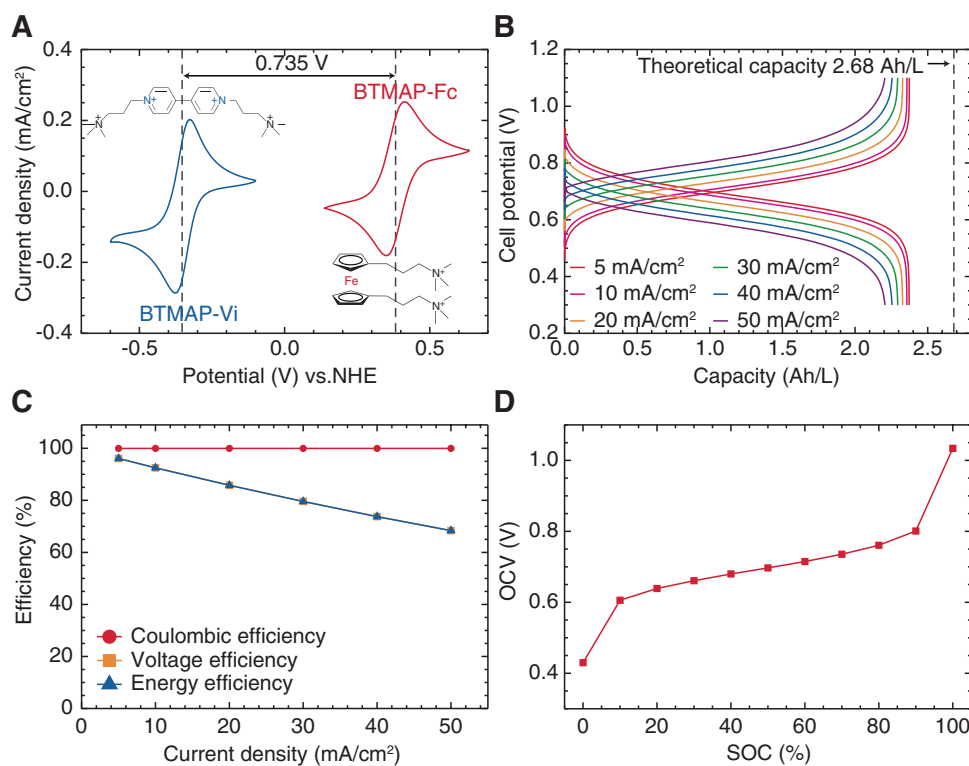
Figure 1. A) Cyclic voltammogram of 5.0×10^{-3} M BTMAP-Fc (red curve) and 5.0×10^{-3} M BTMAP-Vi (blue curve) in 1.0 M NaCl scanned at 10 mV s^{-1} on a glassy carbon electrode, showing a 0.735 V voltage difference. B) Representative galvanostatic cycling curves from 5 to 50 mA cm^{-2} with cutoff voltages of 1.1 and 0.3 V. C) RFB Coulombic efficiency, voltage efficiency, and energy efficiency at different galvanostatic cycling current densities. D) Measured cell open-circuit voltage (OCV) versus state-of-charge (SOC).

operated for photoelectrolysis of water under extreme pH conditions (such as 1 M HClO$_4$ and 1 M KOH) with good stability.[19] Thus, this protection could potentially enable practical long-term operation of Si-based photoelectrodes in neutral electrolytes. Having established the excellent RFB performance with the 0.20 M BTMAP electrolytes, we feed the same electrolytes to SFB device for studying its performance under different operation modes with configurations listed at the bottom of Figure 2A. Briefly, in addition to using only the two inert carbon felt electrodes to perform the RFB tests as described above, we can either pair the photoelectrode with carbon felt electrode on the same cell chamber to turn over and regenerate one pair of redox couple and directly produce electricity (solar cell mode); or connect it with the other photoelectrode in series to store converted solar energy as chemical energy by creating an electrochemical bias between the two BTMAP redox couples (solar recharge mode). The detailed discussion on the operation and chemical reactions under different operation modes is presented in Scheme S1 (Supporting Information).

Figure 2C shows the current density–voltage (J–V) performance of independently characterized photoanode and photocathode configured to solar cell mode with 1 sun (100 mW cm^{-2}) simulated solar illumination provided by a quartz tungsten halogen (QTH) lamp or in the dark. To find an optimal electrolyte flow rate for the SFB, we carried out the linear scan voltammetry with three electrolyte flow rates: 20 mL min^{-1} (MPM), 60 MPM, and 130 MPM. Except for the very slight improvement

in fill factor (FF) at high flow rates, the solar performance of both photoelectrodes appears to be rather insensitive to electrolyte flow rates within the range we studied. Such results indicate that the "zero-gap" device design can ensure sufficient electrochemical mass transport between photoelectrodes and carbon felt electrodes even at a flow rate as low as 20 MPM. At 20 MPM, the photoanode shows an open-circuit voltage (V_{oc}) of 0.559 V and a short-circuit current density (J_{sc}) of 29.4 mA cm^{-2}, and photocathode shows a well-matched V_{oc} of 0.532 V and J_{sc} of 32.8 mA cm^{-2}. The combination of these two photoelectrodes can provide a total V_{oc} of 1.091 V for solar charging the BTMAP SFB device without external bias. We also noticed that, in comparison with the solid-state PV cells fabricated with same type of silicon cells (Figure S2, Supporting Information), the photoelectrodes measured individually under solar cell mode (at 20 MPM) exhibit reasonably preserved V_{oc} and J_{sc} but noticeable decrease in FF (from 64.1 to 51.7% for photoanode and from 69.9 to 38.9% for photocathode), resulting in a lower overall power conversion efficiency for both photoelectrodes (8.49% for photoanode and 6.79% for photocathode). Potentiostatic electrochemical impedance spectroscopy (EIS) was employed to further study the mechanism behind such efficiency loss (Figure S3, Supporting Information). By comparing and analyzing EIS data of the solid-state silicon solar cells and photoelectrodes, we attribute the decrease in FF to the uncompensated solution resistance and nonideal charge extraction process at the semiconductor–liquid interface.
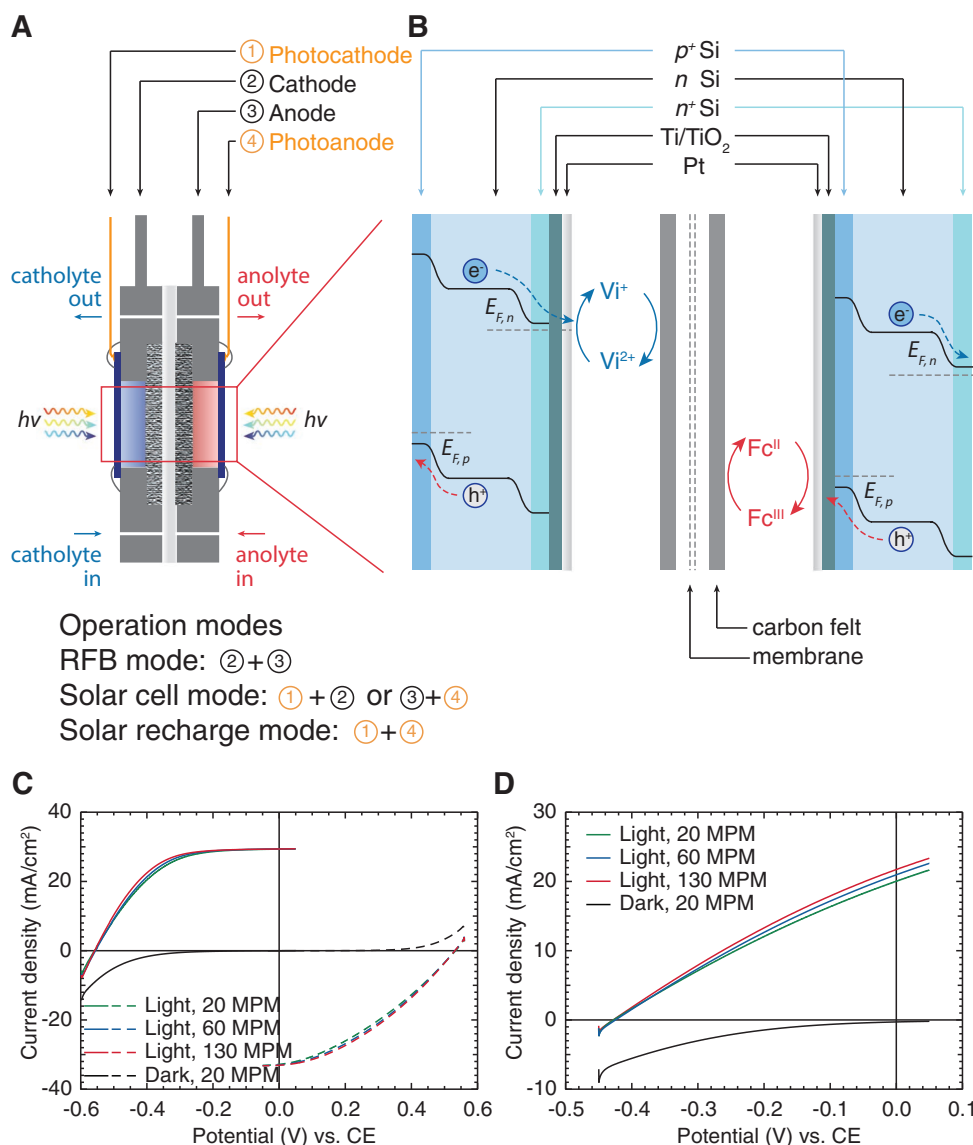
Figure 2. A) Schematic cross section of the SFB, showing two single junction silicon photoelectrodes and two carbon felt inert electrodes, which could be connected in three different modes. B) Zoom-in scheme of the center part in the SFB, illustrating the architectures and energy diagrams of the illuminated photoelectrodes in equilibrium with BTMAP-Vi and BTMAP-Fc redox couples. C) *J–V* performance of the photoanode (solid curves) and photocathode (dashed curves) in 0.2 M BTMAP electrolytes, measured individually under solar cell mode at different flow rates. D) *J–V* performance of photoanode and photocathode connected in series in 0.2 M BTMAP electrolytes, measured under solar recharge mode at different flow rates.

In addition to the *J–V* characterization of individual photoelectrodes measured under solar cell mode, we also investigate the overall solar performance of the SFB device under solar recharge mode by measuring the *J–V* response between photoanode and photocathode (Figure 2D). As illustrated in Figure S4 (Supporting Information), the operating current density of SFB can be found at the intersection point of the overlaid *J–V* curves for independently characterized photoanode and photocathode under solar cell mode. J_{sc} under solar recharge mode equals the operating current density of SFB. The slight increase of J_{sc} under solar recharge mode with increasing flow rates is the cumulative result of aforementioned FF dependence of individual photoelectrodes on flow rate, as the intersection point is on the high curvature region of these *J–V* curves. After

confirming that high flow rates would not bring significant benefits to SFB devices, 20 MPM was selected to perform all studies described hereafter.

The main function of SFBs is capturing and storing solar energy when the sun is shining, and delivering electrical energy on demand. This calls for the cooperation between the solar recharge mode and the RFB mode. In order to demonstrate that the SFB device can be stably operated between these two modes, we performed a long-term cycling test on this device using a synchronized dual channel potentiostat to continuously monitor solar recharge photocurrent and cell potential. Each cycle was started with 1 h of bias-free solar charging by connecting the photoanode and photocathode in series, followed by a galvanostatic discharging step at −5 mA cm⁻² (a current of
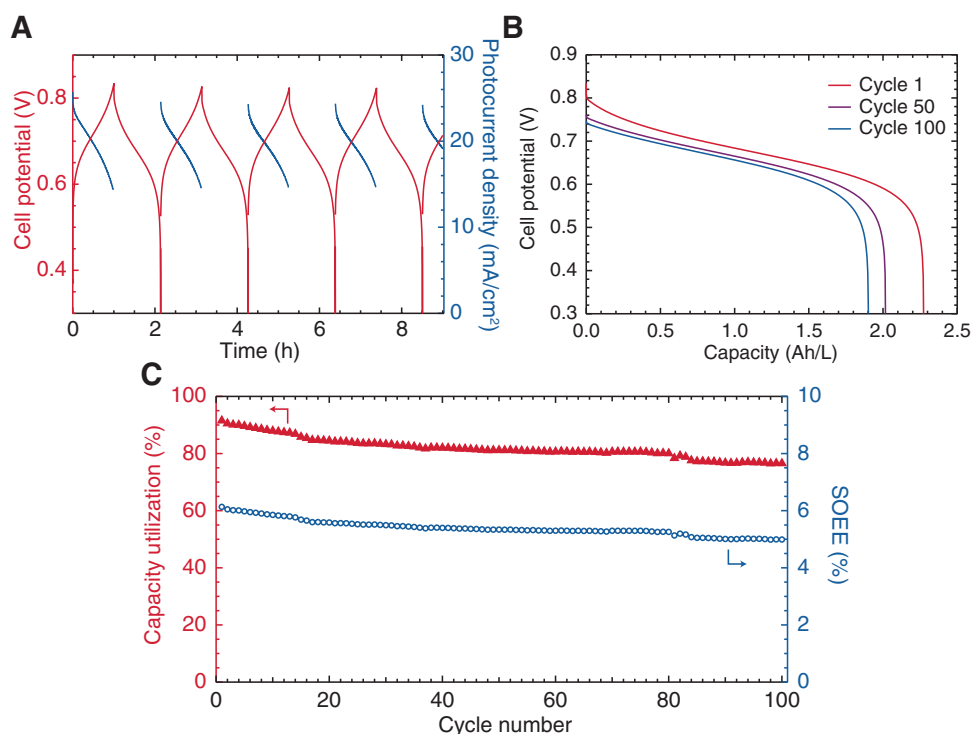
Figure 3. A) Representative device cycling behavior showing cell potential between cathode and anode (red curves), as well as the photocurrent density delivered by the photoelectrodes connected in series (blue curves), recorded between the first and fifth cycles. B) Representative potential–capacity profiles during galvanostatic discharging process at cycle 1, 50, and 100. The capacity shown here represents the effectively utilized capacity at each cycle after solar charging. C) Discharging capacity utilization rate (normalized on the basis of the potentiostatically determined capacity before cycling) and solar-to-output electricity efficiency (SOEE), showing a stable cycling performance over 200 h (100 cycles). Each cycle was started with a 1 h bias-free solar charging process followed by a galvanostatic discharging step at −20 mA until reaching the cutoff potential (0.3 V).

−20 mA, based on a carbon felt electrode area of 4 cm²) until a cutoff potential of 0.3 V was reached. Representative device cycling behavior recorded during the first five cycles of the long-term cycling test is shown in **Figure 3**A. The red curve is the cell potential profile measured between the two carbon felt electrodes. Although this curve resembles the typical voltage–time (V–t) profile of common RFBs, it has a subtle, yet conceptually important difference. Because no external current was provided by the potentiostat during the solar charging process, the rising cell potential recorded during this process represents only the open-circuit potential (E_{oc}, this is the open-circuit potential of the RFB component and should be distinguished from V_{oc} of the photoelectrode) of the SFB without any overpotential, while the descending potential recorded during galvanostatic discharging step can be interpreted as $E_{oc} - \eta$ (η is the overall overpotential), as the case for RFBs. The solar recharge current density (blue curve in Figure 3A) started at ≈24 mA cm⁻² and gradually decreased to ≈15 mA cm⁻² at the end of the 1 h charging cycle due to the increase of cell potential, resulting in an average photocurrent density of 18.5 mA cm⁻² (a current of 22.9 mA, based on an average photoelectrode area of 1.239 cm²). With the relatively high total photovoltage (≈1.1 V) generated by the photoelectrodes, the SFB can effectively utilize most of its storage capacity and reach a near unity state-of-charge (SOC) after being charged for 1 h. The following discharging cycle (cycle 1 in Figure 3B) can deliver a volumetric capacity of 2.27 Ah L⁻¹ (energy density of 1.52 Wh L⁻¹,

calculated based on the total volume of both electrolytes), corresponding to 91.5% of the total potentiostatically determined capacity. Based on the solubility of BTMAP redox couples and RFB study in the previous work, the theoretical capacity for the SFB device is 25 Ah L⁻¹ when 1.9 M of BTMAP redox couples are used.[16c]

Figure 3C shows the SFB can be stably cycled between solar recharge mode and RFB mode over 100 cycles (>200 h) and maintain an average capacity utilization rate of 81.9%. In comparison, the continuous operation durations for all previous SFB demonstrations are less than 50 h.[4a] The round trip energy efficiency of the SFB was evaluated by the SOEE as defined by the following equation

$$\text{SOEE} = \frac{E_{\text{electrical,out}}}{E_{\text{illumination}}} = \frac{\int I_{\text{out}} V_{\text{out}} \mathrm{d}t}{\int SA \mathrm{d}t} \tag{1}$$

where $E_{\text{electrical,out}}$ is the output electrical energy delivered on demand after storage and $E_{\text{illumination}}$ is the input solar energy (calculated based on the total area of both photoelectrodes). The SFB maintained a high SOEE during the long-term cycling test with an average of 5.4%, which is an over twofold increase in comparison to that of the previously demonstrated SFB using the same silicon photoelectrode design (1.7%).[8b] In addition, both Coulombic and voltage efficiency of the SFB were higher than 90% throughout the cycling test (Figure S5, Supporting
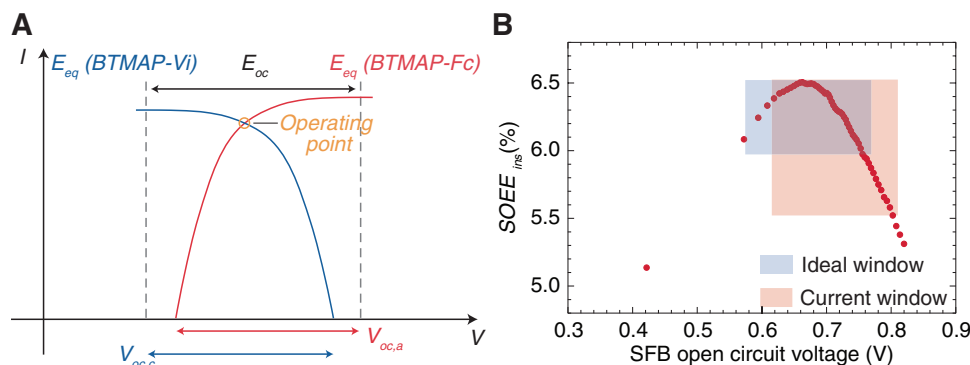
Figure 4. A) Overlaid hypothetical J–V curves of photoanode and photocathode. The intersection point of the red and blue curves is influenced by the RFB voltage. The instantaneous SOEE is determined by the power at the operating point. B) Representative instantaneous SOEE as a function of E_{oc} calculated from the first photocharging cycle of the long-term SFB cycling test shown in Figure 3C. The maximum instantaneous SOEE (6.51%) was achieved at an E_{oc} of 0.663 V (22.6% SOC). The semitransparent shaded areas represent the E_{oc} range between 10% SOC and 90% SOC for a SFB with the current BTMAP redox couples (pink) and hypothetical ideal redox couples that have a formal potential difference of 0.663 V (blue).

Information). Although Figure 3C shows slow decay in the capacity utilization rate and SOEE for the SFB, detailed device characterization after the cycling test (Figure S6, Supporting Information) suggests that such decay could be avoided with a little additional engineering effort. This decay was mainly caused by the decrease of illumination intensity and accumulation of bubbles in the small electrolyte pocket between the photoelectrodes and carbon felt electrodes. These bubbles can block the flow chambers and result in a decrease of effective electrolyte-contacting surface areas for both photoelectrodes and carbon felt electrodes. For both photoanode and photocathode, their J_{sc} under solar cell mode can be significantly increased after replacing the light bulb and recalibrating the illumination intensity of the QTH solar simulator. The decay in photocurrent was also responsible for the decreased capacity utilization rate shown in Figure 3B,C because the solar charging process was set to a constant time (1 h). Additionally, by temporarily increasing the flow rate to 130 MPM to flush out the bubbles accumulated in the flow chambers, we were able to improve the solar performance of the photoelectrodes and almost fully recover it to the original level before the cycling test. Fortunately, bubble accumulation is a minor engineering issue that can be easily solved with some modifications in flow management and therefore will not affect the true stability of the SFB devices (Figure S7, Supporting Information). In addition, the issue of bubble accumulation can also be addressed by using a well-designed flow channel structure to avoid the need for flushing. In fact, the stability of the photoelectrodes was so good that we actually disassembled and reassembled the SFB devices several times for various tests using the same pair of photoelectrodes. The total operation time of these photoelectrodes was well over 400 h.

The long lifetime of the SFB device is enabled by the combination of robust photoelectrodes, stable redox flow battery chemistry, and the careful design of the SFB. From the 200 h cycling test, we did not see an unrecoverable SOEE loss. Based on previous studies on TiO$_2$ protected Si photoelectrodes[20] and BTMAP RFBs,[16c] we think the stability of the photoelectrodes could eventually limit the overall lifetime of the SFB device beyond the thousands of hours in typical lab test settings.

Furthermore, compared to most SFB devices previously demonstrated that could only access a small portion of the total capacity,[4a] the SFB demonstrated here sets a new benchmark for capacity utilization rate, which is an essential quality for practical applications. Being able to solar charge the SFB device to a near unity SOC also brings out another unique aspect of the integrated solar energy conversion and electrochemical storage devices. Unlike conventional PEC devices dealing with redox reactions with fixed equilibrium potentials, such as solar water electrolysis[13b,21] and liquid junction solar cells,[22] SFBs and other similar integrated devices store energy by building up its internal electrochemical potential (E_{oc} increase in Figure 3A).[3a] As illustrated in **Figure 4**A, an increase of E_{oc} would result in a shift of the operating point on the I–V curve of photoelectrodes and consequently cause a change in SOEE. To quantify the relationship between SOEE and E_{oc}, we derive and propose a modified figure of merit, instantaneous SOEE (SOEE$_{ins}$), from Equation (1)

$$\text{SOEE}_{ins} = \frac{P_{electrical,out}}{P_{illumination}} \approx \frac{I_{photo} E_{oc} \times CE \times VE}{SA} \tag{2}$$

where $P_{electrical, out}$ is the discharging power, which is estimated by using charging power $I_{photo} E_{oc}$ times the internal power conversion efficiency of SFB; $P_{illumination}$ is the illumination power provided by the solar simulator. The detailed derivation and explanation can be found in the Supporting Information. SOEE$_{ins}$ can be simply interpreted as the external power conversion efficiency of the SFB device at certain E_{oc}. A representative SOEE$_{ins}$ curve with respect to E_{oc} is presented in Figure 4B, which is numerically calculated from the first solar charging cycle in Figure 3A with a constant time interval of 60 s using cell potential and photocurrent data points that are nearest to the desired time. The SOEE$_{ins}$ increases at the beginning and then decreases as E_{oc} increases, showing a maximum of 6.51% at 0.663 V and an average of 6.15% that is essentially the same as the SOEE value (6.13%) calculated using Equation (1). By plotting E_{oc} with respect to SOC, we can also find that the highest SOEE$_{ins}$ was reached at a SOC of 22.6%. The shaded area in Figure 4B shows the E_{oc} range between 10% SOC and 90% SOC (an example of E_{oc} vs

**ADVANCED
SCIENCE NEWS**
www.advancedsciencenews.com

**ADVANCED
ENERGY
MATERIALS**
www.advenergymat.de

SOC for current BTMAP redox couples is plotted in Figure 1D), which represents the typical operation window for practical SFBs or RFBs. Since the overall SOEE of a SFB device is close to the average $SOEE_{ins}$ value within the shaded E_{oc} window, the highest SOEE with the same photoelectrodes should be achieved under the hypothetical blue area. With this method, we can derive the best matched E_{cell} for SFBs to extract the highest power conversion efficiency out of certain photoelectrodes.

Note that for given photoelectrodes, $SOEE_{ins}$ is only determined by E_{oc}, so the $SOEE_{ins}$–E_{oc} relationship for the same photoelectrodes should remain unchanged no matter which redox couples are used. Thus, the $SOEE_{ins}$–E_{oc} curve can serve as a better guide for tuning the operating $SOEE_{ins}$ window of the SFB with different redox couples in order to optimize the average SOEE. For example, for the p/n Si photoelectrodes used in this study, the best matched E_{cell} should be 0.663 V. As mentioned above, although the same p/n Si photoelectrode design was used, the SFB studied here can deliver a SOEE over three times that of a previous SFB demonstration.[8b] Such enhancement can be readily explained with the knowledge of the $SOEE_{ins}$–E_{oc} relationship for these p/n Si photoelectrodes: E_{cell} for the present SFB (0.735 V) is much closer to the optimized E_{cell} (0.663 V) than that for the previous demonstration (0.461 V).

Although previous report suggested that the SOC dependency of SOEE can be studied by first charging the SFB to desired SOCs and then measuring solar response of the photoelectrode (a set of data using this method is presented in Figure S8, Supporting Information),[8e] the introduction of $SOEE_{ins}$ makes this analysis much easier and more reliable, since the $SOEE_{ins}$–SOC relationship can be directly derived from real-time SFB cycling data without additional tests and undesired SOC disturbance. More importantly, harnessing the $SOEE_{ins}$–E_{oc} relationship (such as Figure 4B), the development of the solar energy conversion and electrochemical energy storage components in SFBs can be decoupled to allow independent optimization of these components. The in-depth study on the $SOEE_{ins}$ unveiled a more flexible design principle for SFBs that can be universally applied to other SFB devices to extract the most solar energy conversion efficiencies out of given solar cells. Such new understanding can stimulate the development of designer solar materials[13a,b,23] and redox species[15b,24] specifically for SFBs.

This work demonstrates that by taking advantage of stable redox couples in low corrosiveness neutral pH electrolytes and well-protected Si photoelectrodes, the lifetime of SFBs can be greatly extended. The extensive studies on Si-based photoelectrodes for PEC energy conversion applications over the last few decades[25] have led to development and demonstration of successful protection strategies for Si-based photoelectrodes in contact with aqueous electrolytes.[19] Indeed, a recent report has shown that np+-Si/TiO2/NiCrOx can drive PEC water oxidation in 1.0 M KOH continuously over three months.[20] This bodes well for SFBs, because the simplified photoelectrode structure without catalysts in SFBs and the less harsh neutral pH condition are expected to further extend the lifetime of Si photoelectrodes. Moreover, as a small bandgap semiconductor (1.1 eV), silicon shows great promises as the bottom layer material for tandem junction solar cells, such as a-Si/μc-Si (amorphous Si/microcrystalline Si) tandem cell[26] and III–V/Si tandem cell,[27] which features not only higher efficiency but also larger photovoltage. The ongoing development of tandem junction PV cell technologies has led to the hope that fabricating additional junctions on single junction Si bottom substrate could be a more cost-effective strategy compared to single junction cells. The decoupled light absorption/solution contact photoelectrode design used in our SFBs (Figure 2B) ensures that these emerging tandem junction cells can be readily adopted into the current SFB design frame to boost its SOEE. In addition, these tandem junction solar cells demand specifically designed redox couples to realize a good voltage match, which can be rationalized under the guidance of $SOEE_{ins}$–E_{oc} relationship.

The SFB device studied in this work sets new records for both continuous operation time (>200 h) and capacity utilization rate (>80%). The successful application of the voltage matching principle yields a significantly boosted SOEE from 1.7 to 5.4% using the same silicon photoelectrode design. In addition, the high capacity utilization rate unveiled the unique SOC dependence of the SOEE for SFBs that differentiates SFBs from other conventional PEC regenerative or electrolysis devices. The newly introduced $SOEE_{ins}$ and the $SOEE_{ins}$–E_{oc} curve can provide guidance toward more efficient SFB device design with better working voltage match between photoelectrodes and redox couples. Building on highly stable BTMAP redox couples and Si photoelectrodes, the long lifetime SFB demonstrated here sets an important milestone to move SFB research into a more practical arena.

Supporting Information

Supporting Information is available from the Wiley Online Library or from the author.

Conflict of Interest

The authors declare no conflict of interest.

Keywords

[1] Z. G. Yang, J. L. Zhang, M. C. W. Kintner-Meyer, X. C. Lu, D. W. Choi, J. P. Lemmon, J. Liu, *Chem. Rev.* **2011**, *111*, 3577.

[2] a) P. Alotto, M. Guarnieri, F. Moro, *Renewable Sustainable Energy Rev.* **2014**, *29*, 325; b) G. L. Soloveichik, *Chem. Rev.* **2015**, *115*, 11533.

**ADVANCED
SCIENCE NEWS**

www.advancedsciencenews.com

**ADVANCED
ENERGY
MATERIALS**

www.advenergymat.de

[3] a) A. Gurung, Q. Q. Qiao, *Joule* **2018**, *2*, 1217; b) B. Luo, D. Ye, L. Wang, *Adv. Sci.* **2017**, *4*, 1700104.

[4] a) K. Wedege, D. Bae, W. A. Smith, A. Mendes, A. Bentien, *J. Phys. Chem. C* **2018**, *122*, 25729; b) A. Gurung, K. Chen, R. Khan, S. S. Abdulkarim, G. Varnekar, R. Pathak, R. Naderi, Q. Q. Qiao, *Adv. Energy Mater.* **2017**, *7*, 1602105.

[5] G. Hodes, J. Manassen, D. Cahen, *Nature* **1976**, *261*, 403.

[6] S. Jin, *ACS Energy Lett.* **2018**, *3*, 2610.

[7] M. Yu, W. D. McCulloch, Z. Huang, B. B. Trang, J. Lu, K. Amine, Y. Wu, *J. Mater. Chem. A* **2016**, *4*, 2766.

[8] a) M. Yu, W. D. McCulloch, D. R. Beauchamp, Z. Huang, X. Ren, Y. Wu, *J. Am. Chem. Soc.* **2015**, *137*, 8332; b) W. Li, H.-C. Fu, L. Li, M. Caban-Acevedo, J.-H. He, S. Jin, *Angew. Chem., Int. Ed.* **2016**, *55*, 13104; c) S. Liao, X. Zong, B. Seger, T. Pedersen, T. Yao, C. Ding, J. Shi, J. Chen, C. Li, *Nat. Commun.* **2016**, *7*, 11474; d) K. Wedege, J. Azevedo, A. Khataee, A. Bentien, A. Mendes, *Angew. Chem., Int. Ed.* **2016**, *55*, 7142; e) K. Wedege, D. Bae, E. Dražević, A. Mendes, P. C. K. Vesborg, A. Bentien, *RSC Adv.* **2018**, *8*, 6331; f) Y. Zhou, S. Zhang, Y. Ding, L. Zhang, C. Zhang, X. Zhang, Y. Zhao, G. Yu, *Adv. Mater.* **2018**, *30*, 1802294; g) Q. Cheng, W. Fan, Y. He, P. Ma, S. Vanka, S. Fan, Z. Mi, D. Wang, *Adv. Mater.* **2017**, *29*, 1700312.

[9] W. Li, H.-C. Fu, Y. Zhao, J.-H. He, S. Jin, *Chem* **2018**, *4*, 2644.

[10] K. A. W. Horowitz, T. Remo, B. Smith, A. Ptak, National Renewable Energy Laboratory, https://www.nrel.gov/docs/fy19osti/72103.pdf (accessed: March 2019).

[11] a) Y. Ding, C. Zhang, L. Zhang, Y. Zhou, G. Yu, *Chem. Soc. Rev.* **2017**, *111*, 3577; b) X. Wei, W. Pan, W. Duan, A. Hollas, Z. Yang, B. Li, Z. Nie, J. Liu, D. Reed, W. Wang, V. Sprenkle, *ACS Energy Lett.* **2017**, *2*, 2187; c) D. P. Tabor, R. Gomez-Bombarelli, L. Tong, R. G. Gordon, M. J. Assiz, A. Aspuru-Guzik, *J. Mater. Chem. A* **2019**, *7*, 12833; d) M. A. Goulet, M. J. Aziz, *J. Electrochem. Soc.* **2018**, *165*, A1466.

[12] a) B. Yang, L. Hoober-Burkhardt, F. Wang, G. K. Surya Prakash, S. R. Narayanan, *J. Electrochem. Soc.* **2014**, *161*, A1371; b) L. Hoober-Burkhardt, S. Krishnamoorthy, B. Yang, A. Murali, A. Nirmalchandar, G. K. S. Prakash, S. R. Narayanan, *J. Electrochem. Soc.* **2017**, *164*, A600.

[13] a) K. Sivula, R. van de Krol, *Nat. Rev. Mater.* **2016**, *1*, 15010; b) M. G. Walter, E. L. Warren, J. R. McKone, S. W. Boettcher, Q. Mi, E. A. Santori, N. S. Lewis, *Chem. Rev.* **2010**, *110*, 6446; c) D. Bae, B. Seger, P. C. K. Vesborg, O. Hansen, I. Chorkendorff, *Chem. Soc. Rev.* **2017**, *46*, 1933.

[14] a) T. W. Hamann, N. S. Lewis, *J. Phys. Chem. B* **2006**, *110*, 22291; b) A. G. Scheuermann, P. C. McIntyre, *J. Phys. Chem. Lett.* **2016**, *7*, 2867.

[15] a) R. M. Darling, K. G. Gallagher, J. A. Kowalski, S. Ha, F. R. Brushett, *Energy Environ. Sci.* **2014**, *7*, 3459; b) J. Winsberg, T. Hagemann, T. Janoschka, M. D. Hager, U. S. Schubert, *Angew. Chem., Int. Ed.* **2017**, *56*, 686.

[16] a) D. G. Kwabi, K. Lin, Y. Ji, E. F. Kerr, M.-A. Goulet, D. De Porcellinis, D. P. Tabor, D. A. Pollack, A. Aspuru-Guzik, R. G. Gordon, M. J. Aziz, *Joule* **2018**, *2*, 1894; b) J. Luo, B. Hu, C. DeBruler, Y. Bi, Y. Zhao, B. Yuan, M. Hu, W. Wu, T. L. Liu, *Joule* **2019**, *7*, 9130; c) E. S. Beh, D. De Porcellinis, R. L. Gracia, K. T. Xia, R. G. Gordon, M. J. Aziz, *ACS Energy Lett.* **2017**, *2*, 639.

[17] B. Hu, C. Seefeldt, C. DeBruler, T. L. Liu, *J. Mater. Chem. A* **2017**, *5*, 22137.

[18] D. S. Aaron, Q. Liu, Z. Tang, G. M. Grim, A. B. Papandrew, A. Turhan, T. A. Zawodzinski, M. M. Mench, *J. Power Sources* **2012**, *206*, 450.

[19] a) B. Seger, T. Pedersen, A. B. Laursen, P. C. K. Vesborg, O. Hansen, I. Chorkendorff, *J. Am. Chem. Soc.* **2013**, *135*, 1057; b) S. Hu, M. R. Shaner, J. A. Beardslee, M. Lichterman, B. S. Brunschwig, N. S. Lewis, *Science* **2014**, *344*, 1005.

[20] M. R. Shaner, S. Hu, K. Sun, N. S. Lewis, *Energy Environ. Sci.* **2015**, *8*, 203.

[21] D. G. Nocera, *Acc. Chem. Res.* **2012**, *45*, 767.

[22] a) P. V. Kamat, K. Tvrdy, D. R. Baker, J. G. Radich, *Chem. Rev.* **2010**, *110*, 6664; b) M. Gratzel, *Nature* **2001**, *414*, 338.

[23] M. A. Green, Y. Hishikawa, E. D. Dunlop, D. H. Levi, J. Hohl-Ebinger, A. W. Y. Ho-Baillie, *Prog. Photovoltaics* **2018**, *26*, 427.

[24] a) M. Park, J. Ryu, W. Wang, J. Cho, *Nat. Rev. Mater.* **2017**, *2*, 16080; b) Y. Ding, C. Zhang, L. Zhang, Y. Zhou, G. Yu, *Chem. Soc. Rev.* **2018**, *47*, 69; c) B. Hu, C. DeBruler, Z. Rhodes, T. L. Liu, *J. Am. Chem. Soc.* **2017**, *139*, 1207; d) C. DeBruler, B. Hu, J. Moss, X. Liu, J. Luo, Y. Sun, T. L. Liu, *Chem* **2017**, *3*, 961.

[25] a) R. M. Candea, M. Kastner, R. Goodman, N. Hickok, *J. Appl. Phys.* **1976**, *47*, 2724; b) K. Sun, S. H. Shen, Y. Q. Liang, P. E. Burrows, S. S. Mao, D. L. Wang, *Chem. Rev.* **2014**, *114*, 8662.

[26] H. Sai, T. Matsui, T. Koida, K. Matsubara, M. Kondo, S. Sugiyama, H. Katayama, Y. Takeuchi, I. Yoshida, *Appl. Phys. Lett.* **2015**, *106*, 213902.

[27] S. Essig, C. Allebe, T. Remo, J. F. Geisz, M. A. Steiner, K. Horowitz, L. Barraud, J. S. Ward, M. Schnabel, A. Descoeudres, D. L. Young, M. Woodhouse, M. Despeisse, C. Ballif, A. Tamboli, *Nat. Energy* **2017**, *2*, 17144.

1900918 (8 of 8)

**ADVANCED
ENERGY
MATERIALS**

Supporting Information

A Long Lifetime Aqueous Organic Solar Flow Battery

Wenjie Li, Emily Kerr, Marc-Antoni Goulet, Hui-Chun Fu, Yuzhou Zhao, Ying Yang, Atilla Veyssal, Jr-Hau He, Roy G. Gordon, Michael J. Aziz, and Song Jin*

Supporting Information

A Long Lifetime Aqueous Organic Solar Flow Battery

Wenjie Li, Emily Kerr, Marc-Antoni Goulet, Hui-Chun Fu, Yuzhou Zhao, Ying Yang, Atilla Veyssal, Jr-Hau He, Roy G. Gordon, Michael J. Aziz, and Song Jin [*]

Supporting Methods

Electrochemical Measurements: Cyclic voltammetry (CV) (Figure 1A) and steady state linear sweep voltammetry (LSV) measurements (Figure S1) were conducted using a Bio-Logic SP-200 potentiostat. A 3 mm diameter glassy carbon disk electrode (MF-2012, BASi for CV and MF-2066 for LSV) was used as the working electrode, which was polished using 0.3 μm and 0.05 μm alumina slurry to mirror polish and washed with deionized water (Milli-Q, 18.2 MΩ cm) and methanol before each test. The glassy carbon electrode was further cleaned electrochemically in 1 M Na_2SO_4 solution (with 1 mM potassium ferrocyanide as internal reference) by swiping potential between -1.0 V and 1.5 V *vs.* reference electrode at 100 mV/s until the peak separation of ferrocyanide/ferricyanide redox couple reaches 60 mV. A custom-made Pt coil electrode (0.5 mm diameter) and a saturated calomel electrode (SCE, CH Instruments) were used as the counter and reference electrode, respectively. The electrolyte consisted of 5 mM of either BTMAP-Fc or BTMAP-Vi and 1.0 M NaCl and was purged with argon before measurements. CV was scanned at a scan rate of 10 mV/s and the formal potential of the redox couples (-0.353 V for BTMAP-Vi and 0.382 V for BTMAP-Fc) were estimated by calculating the average potential between anodic peak and cathodic peak in the CV curves. The uncompensated resistance was determined by measuring the high frequency impendence at 100 kHz, which was then used to compensate the CV curves at an 85% compensation level using EC-Lab software. Electrochemical kinetics of the two redox couples was studied using a rotating disk electrode (BASi, RDE-2) at different rotating speed (Figure S1A-B). LSV was scanned at a scan rate of 10 mV/s. The diffusion coefficient (D) of the oxidized BTMAP-Vi and reduced BTMAP-Fc was calculated using Levich equation, $i_l = 0.62nFAD^{2/3}\omega^{1/2}v^{-1/6}C$, where $n = 1$, $F = 96,485$ C/mol, $A = 0.0707$ cm^2, $C = 5.0$ mM, $v = 0.9380 \times 10^{-2}$ cm^2/s (kinematic viscosity of 1.0 M NaCl at 298 K) and i_l determined

at an absolute overpotential ($|\eta|$) of 200 mV (Figure S1C-D). Koutecký–Levich plots ($1/i$ *vs.* $\omega^{-1/2}$) were used to determine the kinetic currents (i_k) at different overpotentials by extrapolating the fitted $1/i$ *vs.* $\omega^{-1/2}$ lines to $\omega^{-1/2} = 0$. The standard rate constants (k_0) and transfer coefficient (α, reduction reaction) were calculated using the Butler-Volmer equation by linearly fitting a Tafel plot (log i_k *vs. η*) between an $|\eta|$ region of 40-80 mV (Figure S1E-F). The RDE experiments were performed 3 times for each redox couple to obtain the average value for D, k_0 and α.

Fabrication of RFB and Integrated SFB Device: The RFB and SFB measurements were carried out in a custom-made zero-gap device, similar to what was reported previously.[1] Graphite plates (1/8-inch thickness, Tokai Carbon or MWI) with a $20 \times 20 \times 1.2$ mm pocket were used as current collector for RFB devices. Modified current collectors with additional 15×15 mm clearance window at the center of the square pocket were used for SFB devices to allow direct contact between photoelectrode and liquid electrolyte. 4 cm^2 graphite felt electrodes (GFD 3 EA, SIGRACELL®) were pre-treated at 400 ^{o}C in air for 6 h before being used on both sides of the cell. 25×25 mm Selemion DSV (Ashahi Glass Co., Ltd.,) was presoaked in 1.0 M NaCl for more than 24 h before it was used as an anion-exchange membrane. The cell was assembled with four pieces of die cut PTFE sheets (0.04-inch thickness) as gaskets and tightened with eight #10-24 bolts torqued to 4.0 Nm. The electrolytes were pumped through the flow channels by a peristaltic pump (Cole-Parmer Masterflex L/S) via PharMed BPT tubing. 10 mL custom made glass vial with two 4 mm OD electrolyte inlet/out arms were used as electrolyte reservoir. All RFB and SFB measurements were carried out in a custom modified N$_2$ flush box (Terra Universal) with continuous N$_2$ flushing.

General RFB Measurements: 5.0 mL solution of 0.2 M bis((3-trimethylammonio)propyl)ferrocene dichloride (BTMAP-Fc) in 1.0 M NaCl and 5.0 mL solution

of 0.2 M bis(3-trimethylammonio)propyl viologen tetrachloride (BTMAP-Vi) in 1.0 M NaCl were used as anolyte and catholyte, respectively. Both BTMAP-Fc and BTMAP-Vi were synthesized following the method described in the previous report[2] or purchased from TCI America. The electrolyte flow rate was controlled at 20 mL/min for all RFB measurements.

The RFB cycling and polarization performance tests were carried out using a Bio-Logic BP-300 potentiostat. Galvanostatic cycling tests were performed by charging and discharging the device at a desired constant current density with 0.3 V and 1.1 V as the bottom and top potential limits, respectively. A 10s rest at open circuit voltage (*OCV*) was employed between each half cycles. The potentiostatic capacity of the RFB was determined by galvanostatic cycling of the RFB as described above followed by a potential hold at cut-off potentials until the current density reached 1 mA/cm^2. To measure *OCV* of the RFB at different states of charge (SOCs), the battery was galvanostatically charged or discharged with a 10% SOC step and then rested for 2 min to measure the OCV. The 0% SOC and 100% SOC were accessed by the galvnostatic-potentiostatic cycling method described above until the current density reached 1 mA/cm^2 at 0.3 V and 1.1 V, respectively. In the cell polarization characterization, a LSV scan was performed at a scan rate of 100 mV/s. To avoid the disturbance of SOC by LSV scans, the RFB was completely discharged to 0% SOC and then recharged to the specific SOC before each LSV was measured. All the SOCs mentioned in this study were calculated based on potentiostatic capacity. Potentiostatic electrochemical impedance spectroscopy (EIS) measurement of the RFB was performed at 0% SOC, 0.3 V bias with a voltage offset of 10 mV, and frequencies ranging from 100 kHz to 1 Hz (Figure S6D).

Fabrication of Photoelectrode Assembly for the Integrated SFB Device: The fabrication of n^+np^+ and p^+nn^+ silicon solar cells with Ti/TiO$_2$/Pt (5 nm/40 nm/5 nm) protection layers followed the

method previously reported.[3] The photoelectrode assembly for the integrated SFB device characterization was fabricated by affixing a n^+np^+ (for photoanode) or a p^+nn^+ (for photocathode) silicon cell onto a custom-made graphite current collector (described in the SFB device section) by epoxy resin (Hysol 9460) to cover the window of the current collector. The back side of the silicon cell (p^+ side for the n^+np^+ cell or n^+ side for the p^+nn^+ cell) was only physically attached to the current collector without forming an electrical contact. The electrolyte can directly contact the back side of the silicon cell through the window of the current collector and harvest photogenerated charges during SFB device operation in solar recharge mode and solar cell mode. The ohmic contact to photoelectrode was made by attaching a copper foil onto the front side of the cell (n^+ side for the n^+np^+ cell or p^+ side for the p^+nn^+ cell) with Ga/In eutectic mixture (Sigma Aldrich) and fixed with silver paint (Ted Pella, PELCO colloidal silver). The ohmic contact area was sealed by epoxy resin. The geometric area of the exposed silicon cell was determined using calibrated digital images and Adobe Photoshop, which was usually between 1.10 cm^2 and 1.30 cm^2.

Solid State and Photoelectrochemical (PEC) Characterization of Silicon Photoelectrodes: Solid state *J-V* performance of the n^+np^+ and p^+nn^+ silicon cells were measured in a two-electrode configuration by making ohmic contact to the front and back side of the cell. The LSV data was collected using a Bio-Logic SP-200 potentiostat under 1 Sun (100 mW/cm^2) of AM 1.5 G simulated illumination by a Newport Model 91191 Xenon arc lamp solar simulator with a scan rate of 100 mV/s. EIS measurements were performed at V_{oc} of the solid state cells under 1 Sun of simulated solar illumination with a voltage offset of 10 mV, and frequencies ranging from 1 MHz to 1 Hz. A Si photodiode (Thorlabs) was used to calibrate the illumination intensity of the AM 1.5G solar simulator to 100 mW/cm^2.

The PEC characteristics of the silicon photoelectrodes were measured in the assembled SFB device with a Bio-Logic BP-300 potentiostat under 1 Sun (100 mW/cm^2) of simulated solar illumination. The illumination was provided by a Newport Model 67011 quartz tungsten halogen (QTH) light source with a branched flexible silica light guild (Taiopto Mems International Co., LTD.) fed through a N$_2$ flush box and collimated by an OSL2COL convex lens collimation tube (Thorlabs). To calibrate the QTH solar simulator, short circuit current (I_{sc}) of a solid-state p^+nn^+ Si solar cell (~ 1.1 cm^2) was first measured under 1 Sun of AM1.5 G simulated solar light using the Newport 91191 solar simulator, then the QTH solar simulator was calibrated to generate the same I_{sc} using the same solid-state p^+nn^+ Si solar cell. The PEC measurements were performed in a two-electrode configuration under both solar cell mode and solar recharge mode (Figure 2C-D) with the same electrolytes used in the RFB test (0.2 M BTMAP-Fc as anolyte and 0.2 M BTMAP-Vi as catholyte, both with 1.0 M NaCl as supporting electrolyte). To study the influence of SOC on the performance of photoelectrodes, the PEC measurements were carried out at different SOCs by galvanostatically charging the SFB to the desired SOC from 0% SOC. The PEC measurements at 50% SOC were also repeated at different flow rates (Figure 2C-D) to investigate the relationship between mass transport and PEC performance of the photoelectrode. A relatively slow flow rate (20 mL/min) was used for all the other PEC measurements because the PEC performance is insensitive to the flow rate. All LSV curves were recorded at a scan rate of 10 mV/s without correcting for any uncompensated resistance losses. EIS measurements of the individual photoelectrodes were performed under solar cell mode at 50% SOC with a flow rate of 20 MPM. The measurements were performed at V_{oc} of the photoelectrodes under 1 Sun of simulated solar illumination (QTH lamp) with a voltage offset of 10 mV, and frequencies ranging from 100 kHz to 1 Hz.

Integrated SFB Device Characterization: The integrated SFB device was assembled with a photoanode assembly, a photocathode assembly, and all the other components the same as the RFB device described in the previous section. The electrolyte flow rate was controlled at 20 mL/min for all the SFB cycling tests.

To characterize the charging-discharging behaviors of the integrated SFB devices, a Bio-Logic BP-300 bi-potentiostat was used: channel 1 was configured as solar recharge mode to monitor the photocurrent; channel 2 was configured as RFB mode to monitor the potential difference between the two carbon felt electrodes (the connections for different modes are illustrated in Figure 2A). During the solar recharging process, silicon photoanodes and photocathodes were illuminated by the QTH light source/silica light guild at 1 Sun from both sides of the SFB without applying any external bias. Photocharging time was adjusted during the first cycle to make sure >90% of the total capacity can be accessed. During the discharging process, the illumination was blocked by an analog signal regulated beam shutter, and the integrated device was operated as a normal RFB with a discharging current of -20 mA applied by channel 2 until the cell potential reached 0.3 V. The discharging current was selected to match the average solar recharging current. The two potentiostat channels and a beam shutter controller (custom made Arduino based device) were synchronized and controlled by channel 2 with its trigger out/analog out function to enable fully automated SFB device cycling test and ensure stable long-term measurement. The total capacity of the SFB device was also measured by galvanostatic-potentiostatic method before and after SFB cycling test to confirm no significant amount of capacity was lost during cycling.

Calculation of SOEE and SOEE_{ins}: In order to quantitatively evaluate the solar conversion and energy storage efficiency of the integrated SFB device, a specific figure of merit should be

considered: solar-to-output electricity efficiency (SOEE), which is defined by the ratio of the

usable electrical energy delivered by the integrated SFB device ($E_{electrical,out}$) over the total solar

energy input ($E_{illumination}$). The *SOEE* can be calculated using equation 1:[3]

$$SOEE = \frac{E_{electrical,out}}{E_{illumination}} = \frac{\int I_{out} V_{out} dt}{\int SA dt} \qquad (1)$$

where I_{out} is the output (discharging) current, V_{out} is the output voltage, S is the total incident

solar irradiance, which is provided by the QTH light source at 100 mW/cm^2, and A is the total

illumination area of photoanode and photocathode. Note that this *SOEE* is the *round-trip*

efficiency of the delivered electrical energy at any time on demand over the original solar energy

input.

Before going into details about instantaneous *SOEE*, we should firstly examine the break-

down of the energy conversion processes of the SFB device. From solar energy input to electrical

energy output, the SFB device need to perform 3 energy conversion steps: input solar energy to

electrical energy, electrical energy to chemical energy, and chemical energy to output electrical

energy, as summarized in the following equation:

$$SOEE = \frac{E_{electrical,out}}{E_{illumination}} = \frac{E_{electrical,in}}{E_{illumination}} \times \frac{E_{chemical}}{E_{electrical,in}} \times \frac{E_{electrical,out}}{E_{chemical}}. \qquad (2)$$

Because the chemical energy of redox couples, $E_{chemical}$, is difficult to quantify, we can rewrite

Equation 3 as follows:

$$SOEE = \frac{E_{electrical,out}}{E_{illumination}} = \frac{E_{electrical,in}}{E_{illumination}} \times \frac{E_{electrical,out}}{E_{electrical,in}}, \qquad (3)$$

where $\frac{E_{electrical,in}}{E_{illumination}}$ is the efficiency for the PEC solar energy conversion component and

$\frac{E_{electrical,out}}{E_{electrical,in}}$ is the efficiency for the electrochemical energy storage component. Because storing

and releasing electrical energy electrochemically only involves turning over redox couples inside

the SFB device, the isolated term, $\frac{E_{electrical,out}}{E_{electrical,in}}$, can be seen as the "internal efficiency" of SFB

and accordingly *SOEE* is the external efficiency of SFB. Note that this internal efficiency of SFB

is completely different from the internal quantum efficiency (IQE) commonly used to evaluate

solar cells.

The hypothetical overlaid *J-V* curves of photoelectrodes shown in Figure 4A illustrates

that the operating point for the integrated SFB device could be significantly influenced by the

working voltage matching between the photoelectrode and the SFB cell potential. Even though

the photovoltage generated by the internal solid-state *p-n* junction of the photoelectrode is

constant, the SFB cell potential may vary greatly during its charging/discharging process,

resulting in a considerable *SOEE* change at different SOCs. To quantitatively analyze such *SOEE*

change at different charging/discharging state of the SFB, an instantaneous *SOEE* can be defined

and estimated using the following equation:

$$SOEE_{ins} = \frac{P_{electrical,out}}{P_{illumination}} \approx \frac{P_{electrical,in} \times PE_{internal}}{P_{illumination}} = \frac{I_{photo}E_{oc} \times PE_{internal}}{SA} \approx$$

$$\frac{I_{photo}E_{oc} \times CE \times VE}{SA}$$

where $P_{electrical,in}$, $P_{eletrical,out}$ and $P_{illumination}$ are the electrical charging power of the SFB, electrical

discharging power of the SFB and illumination power provided by the solar simulator; $PE_{internal}$

is internal power conversion efficiency of the SFB, which can be estimated as the arithmetic

product of Coulombic efficiency (*CE*) and voltage efficiency (*VE*) of the SFB; I_{photo} is

photocurrent density provided by the photoelectrodes during solar recharging process and E_{oc} is

the corresponding cell potential measured at the same time as I_{photo}. An example of $SOEE_{ins}$ vs.

E_{oc} is plotted in Figure 4B.

Table S1. Representative early demonstrations of integrated solar rechargeable battery and recent demonstrations of solar flow batteries (SFBs)

Year	Photoelectrode	Redox species	Photovoltage at open circuit (V)	Cell voltage (V)*	SOEE (%)*	Continuous cycling time (h)
Early demonstrations of integrated solar rechargeable battery						
1976[4]	CdSe	Ag/Ag_2S, S^{2-}/S	0.45-0.56	0.24	<1.2[c]	15
1987[5]	Cd(Se,Te)	Sn/SnS, polysulfide	~0.65	0. 48	11.3[d]	48
Recent demonstrations of SFBs						
2013[6]	TiO_2-dye (DSSC)	$DMFc^{0/+}$, I^-/I_3^-	<0.7	0.7	0.05	~20
2015[7]	TiO_2-Z907 dye (DSSC)	Li/Li^+, I^-/I_3^-	~0.52	3.5	<0.35	29.2
2016[8]	n/p Si PV×2	$AQDSH_2/AQDS$, Br^-/Br_3^-	1.0	0.89	3.2	~10
2016[3]	n/p Si PV×2	$AQDSH_2/AQDS$, $BQDSH_2/BQDS$	1.1	0.45	1.7	10
2016[9]	α-Fe_2O_3	$AQDSH_2/AQDS$, $Fe(CN)_6^{4-/3-}$	~0.60	0.74	<0.08	n/a
2017[10]	Ta_3N_5, GaN-n/p Si PV	$DHAQH_2/DHAQ$, $Fe(CN)_6^{4-/3-}$	1.4	1.2	<3.0	~10
2018[11]	n/p Si PV	$Fe(CN)_6^{4-/3-}$, $[TEMPO-sulfate]^{0/+}$	0.52	0.35	<1.6	7
2018[12]	WO_3-$BiVO_4$	I^-/I_3^-, Br^-/Br_3^-	~1.0	0.55	1.25	>20
2018[1]	InGaP/GaAs/Ge PV	$MV^{+/2+}$, $[4-OH-TEMPO]^{0/+}$	2.41	1.25	14.1	8
This work	n/p Si PV×2	$BTMAP-Vi^{3+/4+}$, $BTMAP-Fc^{2+/3+}$	1.09	0.735	5.4	200

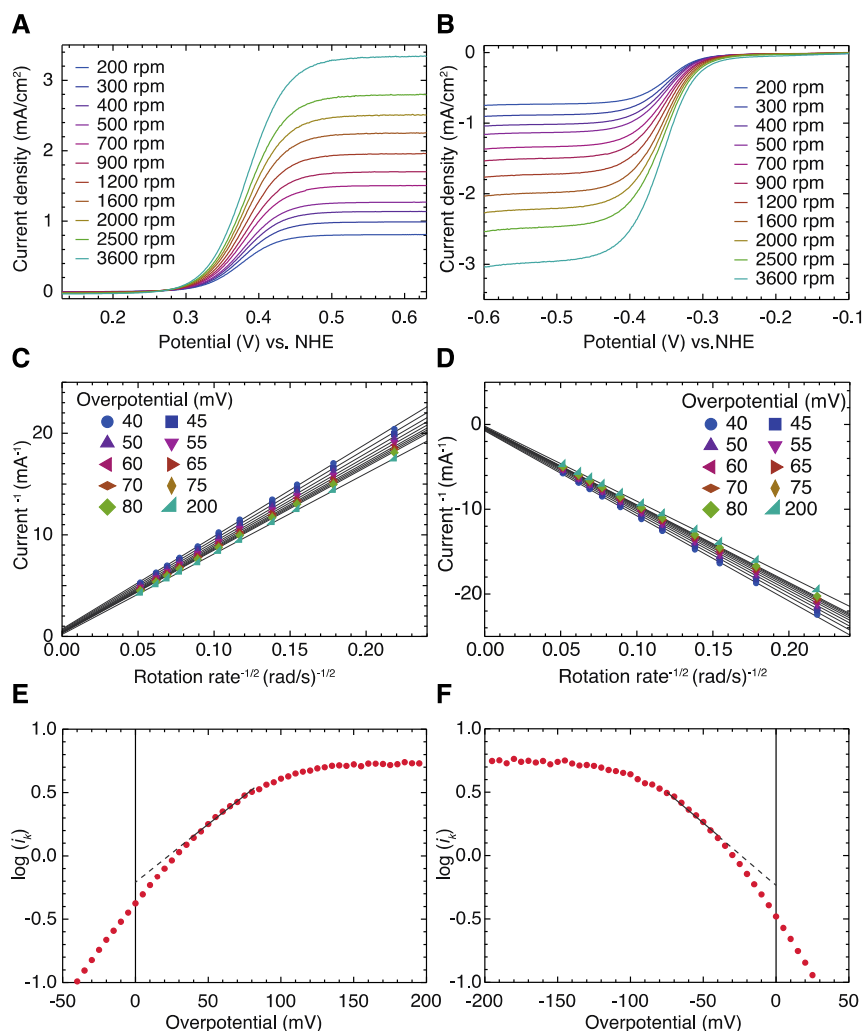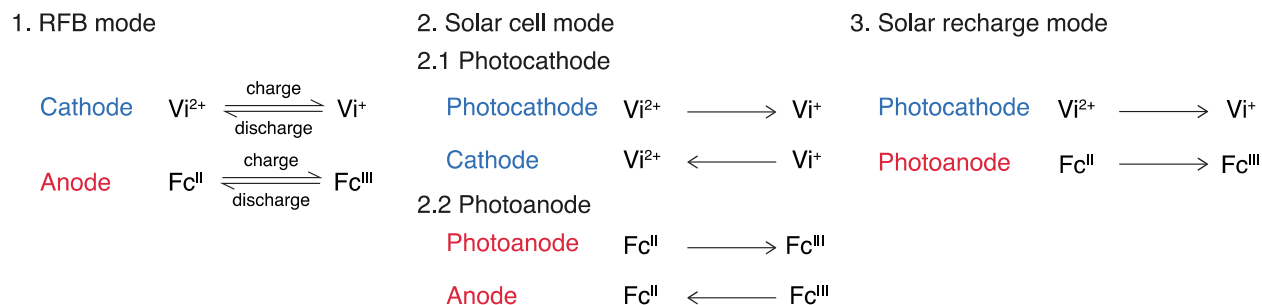*Cell voltage and *SOEE* data are adopted from a previous paper.[1]

Figure S1. LSV curves of 5.0 mM BTMAP-Fc (A) and 5.0 mM BTMAP-Vi (B) in 1.0 M NaCl with a 3.0 mm diameter glassy carbon working electrode rotating at different rates. (C-D) Koutecký–Levich plots derived from (A-B) by extracting disk current at different overpotentials (η). Kinetic current (i_k) can be found by extrapolating the fitted $1/i$ *vs.* $\omega^{-1/2}$ lines to $\omega^{-1/2} = 0$. The slopes at $\eta = 200$ mV were used to calculate the diffusion coefficients of BTMAP-Fc and BTMAP-Vi based on the Levich equation. For BTMAP-Fc, $D_R = 5.3 \times 10^{-6}$ cm^2/s; for BTMAP-Vi, $D_O = 4.8 \times 10^{-6}$ cm^2/s. (E-F) Tafel plots of BTMAP-Fc (E) and BTMAP-Vi (F). The absolute overpotential ($|\eta|$) region between 40-80 mV was linearly fitted to calculate the standard rate constant (k_0) and transfer coefficient (α) based on the Butler-Volmer equation. For BTMAP-Fc, $k_0 = 1.8 \times 10^{-2}$ cm/s and $\alpha = 0.47$; for BTMAP-Vi, $k_0 = 1.6 \times 10^{-2}$ cm/s and $\alpha = 0.49$.

1. RFB mode

Cathode Vi^{2+} $\underset{\text{discharge}}{\overset{\text{charge}}{\rightleftharpoons}}$ Vi^+

Anode Fc^{II} $\underset{\text{discharge}}{\overset{\text{charge}}{\rightleftharpoons}}$ Fc^{III}

2. Solar cell mode

2.1 Photocathode

Photocathode Vi^{2+} $\longrightarrow$ Vi^+

Cathode Vi^{2+} $\longleftarrow$ Vi^+

2.2 Photoanode

Photoanode Fc^{II} $\longrightarrow$ Fc^{III}

Anode Fc^{II} $\longleftarrow$ Fc^{III}

3. Solar recharge mode

Photocathode Vi^{2+} $\longrightarrow$ Vi^+

Photoanode Fc^{II} $\longrightarrow$ Fc^{III}

Scheme S1. Operation principles and reactions under different operation modes. Under RFB mode, the SFB device can be charged and discharged by a potentiostat like a normal RFB device to store and redeliver electrical energy on demand. Under solar cell mode, the photoelectrode is paired with carbon felt electrode in the same cell chamber to turn over and regenerate one pair of redox couple (BTMAP-Vi or BTMAP-Fc) and directly produce electricity. Both photoanode and photocathode can be operated independently under this mode. Under solar recharge mode, photoanode and photocathode are connected in series to store converted solar energy as chemical energy by creating an electrochemical bias between the two BTMAP redox couples.
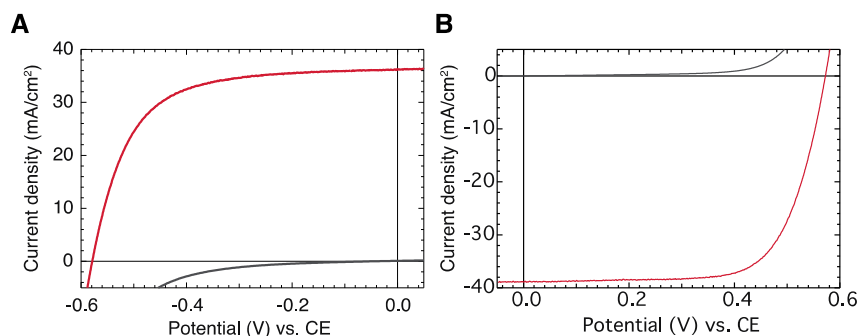
Figure S2. *J-V* performance of the solid-state silicon solar cells under 1 sun (AM 1.5 G) illumination (red) and in the dark (gray): (A) n^+np^+ silicon cell, used to fabricate photoanode, with a power conversion efficiency of 13.5%; (B) p^+nn^+ silicon cell, used to fabricate photocathode, with a power conversion efficiency of 15.6%.
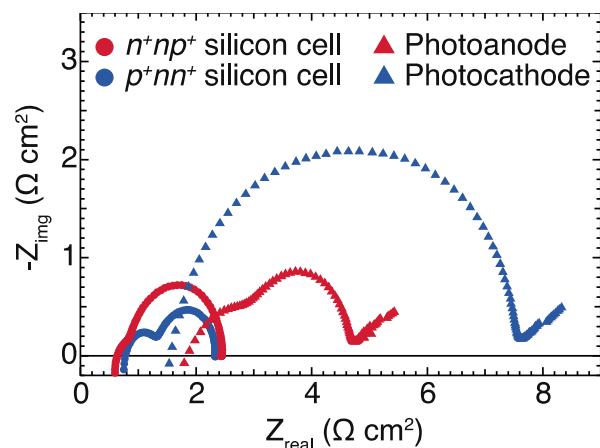
Figure S3. Potentiostatic electrochemical impedance spectroscopy (EIS) of the solid state cells and photoelectrodes are measured under an illumination intensity of 100 mW/cm^2 (1 Sun) at open circuit voltage. Photoelectrodes are characterized individually under solar cell mode.
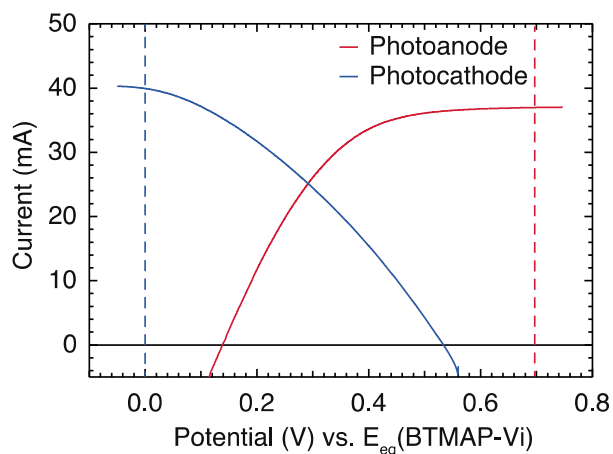

Figure S4. Overlaid *J-V* curve for the photoanode and photocathode measured under solar cell mode. Dashed lines showed the equilibrium potentials (E_{eq}) of BTMAP-Fc (red) and BTMAP-Vi (blue) with respect to the E_{eq} of BTMAP-Vi at 50% SOC. Because these *J-V* measurements were carried out with the 2-electrode set-up, the exact potential with respect to SHE cannot be accurately determined. The intersection of the two *J-V* curves shows the operating point of the photoelectrode at current SOC.
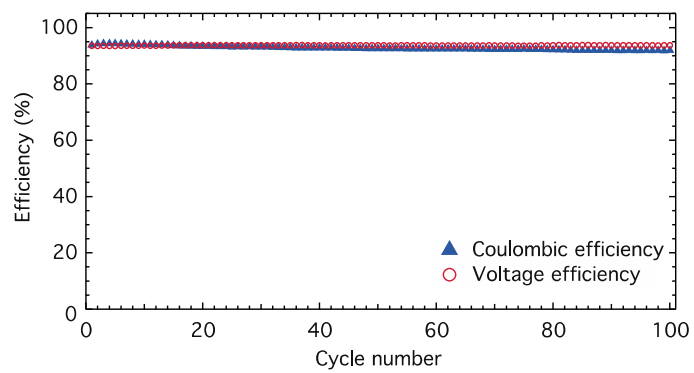
Figure S5. Cycling efficiency plots of the integrated SFB device: coulombic efficiency (blue triangles) and voltage efficiency (red circles).
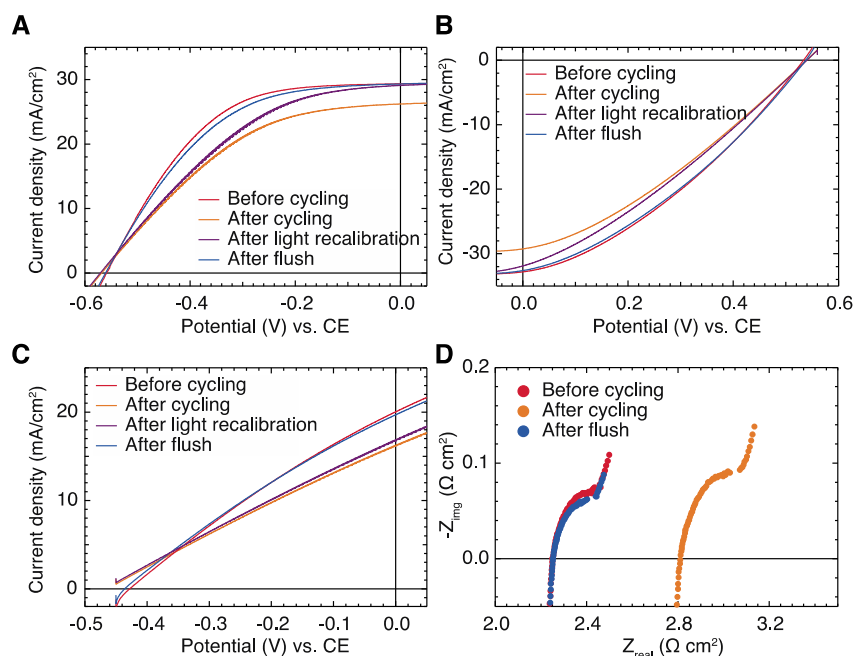
Figure S6. Characterization of the SFB device after long term cycling test. The SOEE drop is mainly caused by two reasons: first, slow decay of illumination intensity of the light source from 1 sun (before cycling) to 0.90 sun (after cycling) over 200 h of continues operation; second, bubble accumulation in the SFB chamber, blocking active surface area of photoelectrodes and graphite felt electrodes. After replacing the light bulb, recalibrating the illumination intensity and flushing the SFB at a high flow rate of 130 mL/min (MPM) for 5 mins, the solar performance can be almost fully recovered. *J-V* performance of the photoanode (A) and photocathode (B), measured individually under solar cell mode at different stage of the whole set of tests. (C) *J-V* performance of the photoanode and photocathode connected in series, measured under solar recharge mode at different stage of the whole set of tests. (D) Potentiostatic EIS measured between two RFB current collectors shows significant increase in r_{hf} after the cycling test, which can be completely restored to the original value after a simple flushing process. This proved the hypothesis of bubble accumulation in the SFB cell during cycling test.
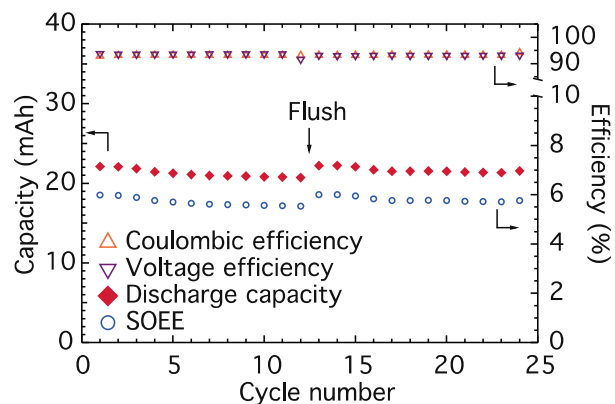
Figure S7. Cycling performance of the integrated SFB device with increased flow rate at 10 cycles intervals. The SFB device was flushed using 130 MPM for 5 min at the end of the 12th cycle. The cycling profile shows that the performance of the SFB device can be easily restored with this quick flush procedure, indicating the slight SFB performance decay could be avoided with better flow management and device engineering.
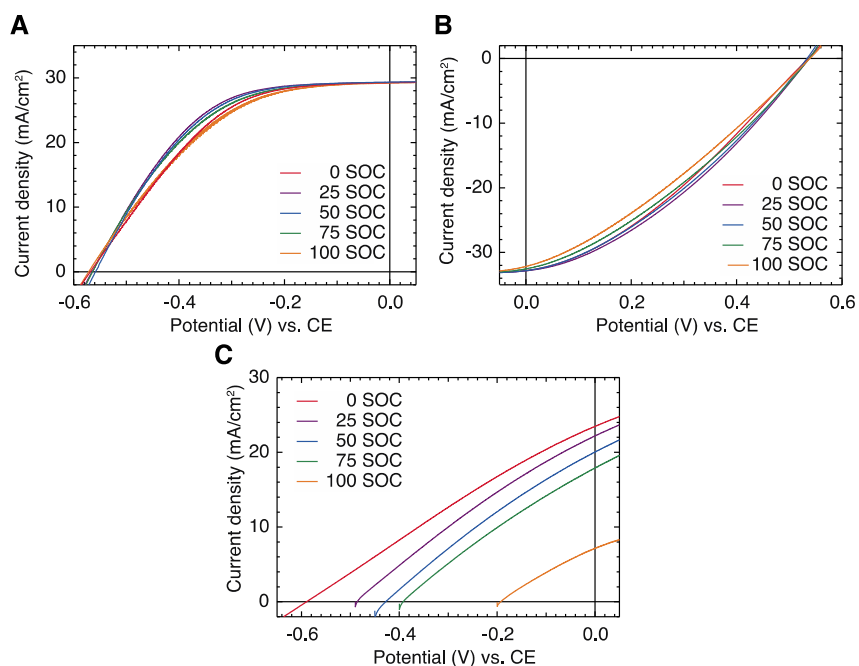
Figure S8. Solar performance of the photoelectrode at different SOCs. To perform the measurements at different SOCs, the SFB was first discharged to 0% SOC and then charged to the desired SOC level using potentiostat to avoid the influence of *J-V* measurements on SOC. *J-V* performance of the photoanode (A) and photocathode (B), measured individually under solar cell mode at 20 MPM. Although the overall solar performance of the individual photoelectrodes are rather insensitive to the SOC changes, the change of fill factor (*FF*) at different SOCs is quite distinguishable. Both photoelectrodes show the best *FF* at 25% SOC and worst *FF* at 100% SOC. (C) *J-V* performance of the photoanode and photocathode connected in series, measured under solar recharge mode at 20 MPM. The overall solar performance under solar recharge mode changed significantly at different SOCs, as illustrated in Figure 4.

References

[1]   W. Li, H.-C. Fu, Y. Zhao, J.-H. He, S. Jin, *Chem* **2018**, *4*, 2644.
[2]   E. S. Beh, D. De Porcellinis, R. L. Gracia, K. T. Xia, R. G. Gordon, M. J. Aziz, *ACS Energy Lett.* **2017**, *2*, 639.
[3]   W. Li, H.-C. Fu, L. Li, M. Caban-Acevedo, J.-H. He, S. Jin, *Angew. Chem. Int. Ed.* **2016**, *55*, 13104.
[4]   G. Hodes, J. Manassen, D. Cahen, *Nature* **1976**, *261*, 403.
[5]   S. Licht, G. Hodes, R. Tenne, J. Manassen, *Nature* **1987**, *326*, 863.
[6]   P. Liu, Y. l. Cao, G. R. Li, X. P. Gao, X. P. Ai, H. X. Yang, *Chemsuschem* **2013**, *6*, 802.

[7] M. Yu, W. D. McCulloch, D. R. Beauchamp, Z. Huang, X. Ren, Y. Wu, *J. Am. Chem. Soc.* **2015**, *137*, 8332.

[8] S. Liao, X. Zong, B. Seger, T. Pedersen, T. Yao, C. Ding, J. Shi, J. Chen, C. Li, *Nat. Commun.* **2016**, *7*, 11474.

[9] K. Wedege, J. Azevedo, A. Khataee, A. Bentien, A. Mendes, *Angew. Chem. Int. Ed.* **2016**, *55*, 7142.

[10] Q. Cheng, W. Fan, Y. He, P. Ma, S. Vanka, S. Fan, Z. Mi, D. Wang, *Adv. Mater.* **2017**, *351*, 1700312.

[11] K. Wedege, D. Bae, E. Dražević, A. Mendes, P. C. K. Vesborg, A. Bentien, *RSC Adv.* **2018**, *8*, 6331.

[12] Y. Zhou, S. Zhang, Y. Ding, L. Zhang, C. Zhang, X. Zhang, Y. Zhao, G. Yu, *Adv. Mater.* **2018**, *103*, 1802294.